

NANO EXPRESS

Open Access



Multi-functional Device with Switchable Functions of Absorption and Polarization Conversion at Terahertz Range

Lin Peng^{1,2*} , Xing Jiang¹ and Si-min Li^{1,3}

Abstract

Terahertz electromagnetic (EM) wave components usually have a single function, such as they can only convert the polarization state of an incident wave or absorb the incident energy, which would be a limitation for their applications. To make a breakthrough, a multi-functional device (MFD) is proposed in this paper, and it is capable of switching between absorption mode and polarization conversion mode. The device has a low-profile and simple structure, and it is constructed by graphene-based absorbing metasurface (AM) and gold-based polarization conversion metasurface (PCM). By controlling the chemical potential (μ_c) of the graphene, the leading role is transferred between the AM and the PCM, which leads to steerable absorption and polarization conversion (PC) modes. For the PC mode, the simulated polarization conversion ratio (PCR) is larger than 0.9 in the 2.11–3.63-THz band (53.0% at 2.87 THz). For the absorption mode, the simulated absorptivity is larger than 80% in the 1.59–4.54-THz band (96.4% at 3.06 THz). The physical mechanisms and operating characteristics of the MFD are discussed. This research has potential applications in terahertz imaging, sensors, photodetectors, and modulators.

Keywords: Absorption mode, Polarization conversion mode, Terahertz, Graphene, Metasurface

Introduction

Absorbers and polarization converters, capable of regulating electromagnetic (EM) wave, are two crucial devices for terahertz technology. They have significant applications in sensors, photodetectors, and modulators, and they are indispensable in medical imaging/diagnostics, environmental monitoring and surveillance, chemical spectroscopy, high-resolution radar, and high-speed communication [1–4]. The absorbers are utilized to absorb and dissipate the impinging EM wave, while the polarization converters have the capacity of polarization state regulating of the illuminating wave. These devices are widely studied in recent years [4–24].

Metasurfaces are found to have perfect absorption in the terahertz wave range [5–8]. This metasurface can be constructed by gold patterns or graphene patterns. The

gold patterns include coupled ring resonator and cross-shaped structure [5], cross-shaped gold resonator [6], and three-layer cross-shaped gold resonators [9]. However, the bandwidths of these gold metasurface absorbers are quite narrow. Graphene, which supports surface plasmons in the terahertz range [10, 11], is a good material to design metasurface-based absorber with a wide bandwidth. The fishnet graphene pattern achieves a bandwidth of 59.4% at 3.2 THz [12], the dual-ring structure with hybridized plasmonic resonances obtains a bandwidth of 1.18–1.64 THz (32.6%) [13], the nine layers of different size graphene ribbons realizes good absorption from 3 to 7.8 THz (88.9%) [14], and the three-layer asymmetrically pattern graphene strips etched with holes in [15] has a bandwidth of 84.6% (4.7–11.6 THz). Though the monolayer of transition metal dichalcogenides and periodic metal nano-groove array has a narrow bandwidth, it absorbs light in a wide angle [16]. In [17], monolayer MoS₂ is applied to titanium nitride nano-disk array, which achieves an average absorption of 98.1% in the band from 400 to 850 nm (72%).

On the other hand, metasurfaces have high performance in polarization conversion. Noble metals, such as gold, have

* Correspondence: penglin@guet.edu.cn; penglin528@hotmail.com

¹Guangxi Key Laboratory of Wireless Wideband Communication and Signal Processing, Guilin University of Electronic Technology, Guilin 541004, Guangxi, China

²School of Physics, University of Electronic Science and Technology of China, Chengdu 541004, China

Full list of author information is available at the end of the article

high efficiency for metasurface-based polarization converter designing. Double L-shaped pattern with two metallic gratings in [18] rotates a linear polarization (LP) by 90°. The bandwidth of the converter in [18] is 0.2–0.4 THz (66.7%). Double L-shaped pattern and grating with Fabry-Perot-like resonance achieve a bandwidth from 0.55 to 1.37 THz (85.4%) [19]. Three-layer metasurfaces form a quarter-wave converter to convert a LP incident wave to a circular polarization (CP) wave, in a bandwidth of 2.1–8 THz (116.8%) [20]. The strip-loaded half elliptical ring structure in [21] is capable of cross-polarization converting both LP and CP with a bandwidth of 2.1–2.9 THz (32%). The graphene metasurfaces applied for polarization converter usually realize the function of frequency or polarization state tuning. The designs in [22, 23] obtain polarization rotation by etching slots/hollows periodically on graphene sheets, and the operating frequencies can be dynamically tuned by adjusting the chemical potential (μ_c). The periodic graphene patterns [24] and dual crossed graphene gratings [25] tune the polarization states. The design in [21] applies graphene strips on the ground to disturb the field distributions; then, the polarization conversion ratio can be regulated.

Though the above-reported absorbers and polarization converters are very efficient, these devices are a single function. They are not accommodated with terahertz systems that require portable, compact, and multi-functional devices. Therefore, multi-functional devices (MFDs) are significant. In this research, an MFD, capable of switching between absorption mode and polarization conversion mode, is proposed. The proposed MFD has a low-profile and simple structure by assembling a gold-based polarization conversion metasurface (PCM) and a graphene-based absorbing metasurface (AM). Then, by setting the chemical potential of graphene $\mu_c = 0$ eV, the AM is neutralized and the PCM plays a dominant role, and the device rotates the polarization of an incident EM wave. By setting $\mu_c = 0.7$ eV, the AM takes the main role and the device absorbs the incident EM wave.

Methods

To obtain the capacity of switching between absorption and polarization conversion (PC) modes, the MFD includes two categories of metasurfaces as shown in Fig. 1. One type is absorbing metasurface (AM), and the other type is PC metasurface (PCM). A typical configuration of the MFD, as presented in Fig. 1, includes PCM structure, AM structure, metallic mirror, and insulators to separate them. It is supposed that, at the absorption mode, the AM dominates the impinging wave and dissipates the incident power, and the PCM is of no avail at this mode. At the PC mode, the AM should be neutralized and the PCM plays a leading role; therefore, the polarization state of the incident wave is converted. To attain the above claims, the key point is the

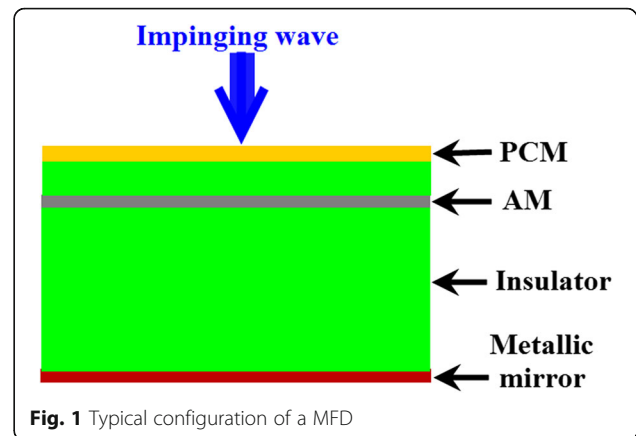


Fig. 1 Typical configuration of a MFD

neutralization of the AM at the PC mode. Therefore, the tunable material should be used to construct the AM, in which the properties of the AM can be tuned. Fortunately, the graphene demonstrates ultra-high electronic mobility and tunable conductivity by adjusting its doping level or electrical grating [26, 27]. Therefore, it is advisable to utilize graphene for AM designing. The conductivity of the graphene can be expressed by Kubo formula (1), and it includes intraband and interband contributions.

$$\begin{aligned}\sigma_s &= \sigma_{\text{intra}}(\omega, \mu_c, \Gamma, T) + \sigma_{\text{inter}}(\omega, \mu_c, \Gamma, T) \\ \sigma_{\text{intra}}(\omega, \mu_c, \Gamma, T) &= -j \frac{e^2 k_B T}{\pi \hbar^2 (\omega - j2\Gamma)} \left(\frac{\mu_c}{k_B T} + 2 \ln \left(e^{\frac{\mu_c}{k_B T}} + 1 \right) \right) \\ \sigma_{\text{inter}}(\omega, \mu_c, \Gamma, T) &\approx -j \frac{e^2}{4\pi \hbar} \ln \left(\frac{2|\mu_c| - (\omega - j2\Gamma)\hbar}{2|\mu_c| + (\omega - j2\Gamma)\hbar} \right)\end{aligned}\quad (1)$$

where e , \hbar , k_B , T , and μ_c represent the charge of an electron, the reduced Planck's constant, Boltzmann's constant, Kelvin's temperature, and chemical potential, respectively. The Γ is a phenomenological scattering rate, and it is assumed to be independent of energy ε . Thus, the complex conductivity σ_s can be adjusted by tuning the chemical potential (μ_c) with biasing voltage. It is found in Eq. (1) that for $\mu_c = 0$ eV, the conductivity of the graphene is very small owing to the low carrier density at this case. Therefore, the graphene operates as a dielectric substrate. Moreover, as the graphene layer is very thin, it has little impact on the illuminated EM waves for $\mu_c = 0$ eV. However, the carrier density of the graphene would be raised with increasing chemical potential (μ_c), and the complex conductivity (σ_s) of the graphene is boosted with increasing chemical potential (μ_c) [26, 27]. Therefore, the graphene supports surface plasmon polaritons (SPPs) for large μ_c [26, 28–30], and the SPPs confine the incident waves. To further enhance the SPPs and achieve wave absorption in certain frequencies, periodical structures should be etched in the graphene layer to form a metasurface, which is called AM. Therefore, by setting $\mu_c = 0$, the

AM can be deemed as a thin dielectric substrate, and it is almost transparent to EM wave. Thereby, the incident EM wave can be concentrated on the PCM layer, and the device operates in the PC mode. For an appropriate large μ_c , the enhanced SPPs of the AM confine most of the incident EM wave, which makes the PCM layer of no avail. Thereby, the incident EM waves are dissipated in the AM layer.

According to the above discussion, a low-profile MFD with gold-based PCM and graphene-based AM is proposed as shown in Fig. 2. Figure 2a is a 3D view of a cell. It is found in the figure that one layer of gold-based PCM is printed on the top of the substrate TOPAS polymer [31]. The PCM pattern is a dual L-shaped structure with wide band and good polarization conversion characteristics [18, 19]. As demonstrated in Fig. 2a, a graphene-based AM is inserted in the TOPAS polymer substrate with a distance h_1 to the PCM. To endow the graphene-based AM a dominant role at the absorption mode, the AM should have strong SPPs at a certain chemical potential (μ_c) to confine most of the incident power and neutralize the PCM. For this purpose, patterns of cross-slots are etched in a graphene layer, as exhibited in Fig. 2b. It is supposed that the cross-slot patterns bring periodic changing ($\sigma = 0$) to the uniformity complex conductivity of the graphene, which leads to charge density rearranging and focusing. Therefore, SPPs are generated and enhanced. The cross-slot structure, as demonstrated in Fig. 2b, is capable of concentrating carrier and fields around the slots, which ensures strong SPPs. The slot lengths of l_1

and l_2 are choosing to ensure the resonances of the AM fall into operating scope of the PCM; therefore, one cell of the AM has 3×3 cross-slot patterns. Note that the PCM and AM are moving and operating independently as their on-off is controlled by the chemical potential (μ_c); therefore, the PCM pattern and the AM pattern could be other architectures. The TOPAS polymer is an excellent substrate material for broadband terahertz design, and its refraction index is approximately 1.53 with a very low loss. A gold layer is printed at the bottom of the TOPAS polymer substrate for total reflection. The gold layer is supported by a substrate, which can be Si. The thickness of the gold is 200 nm. Note that the supporting material has no effect on the performances on the MFD as there are no impinging waves penetrating the gold layer. As demonstrated from a 3D view of the array in Fig. 2c, the chemical potential can be adjusted through biasing the voltage. The MFD can be fabricated by repeating the growth and transfer process [32, 33]. The graphene AM is supposed to have $T = 300$ K and momentum relaxation time $\tau = 0.1$ ps. For PC mode, $\mu_c = 0$ eV. The chemical potential for absorption mode is $\mu_c = 0.7$ eV. The optimized parameters of the MFD are $h_0 = 17$ μm , $h_1 = 1.5$ μm , $l_0 = 24$ μm , $W_0 = 2$ μm , $l_1 = 14$ μm , $l_2 = 19.8$ μm , and $p = 50$ μm .

Results, Physical Mechanisms, and Discussion

Results

The proposed MFD was simulated, and the polarization conversion ratio (PCR) and the absorptivity of the proposed MFD were calculated. As shown in Fig. 3a, the full-wave

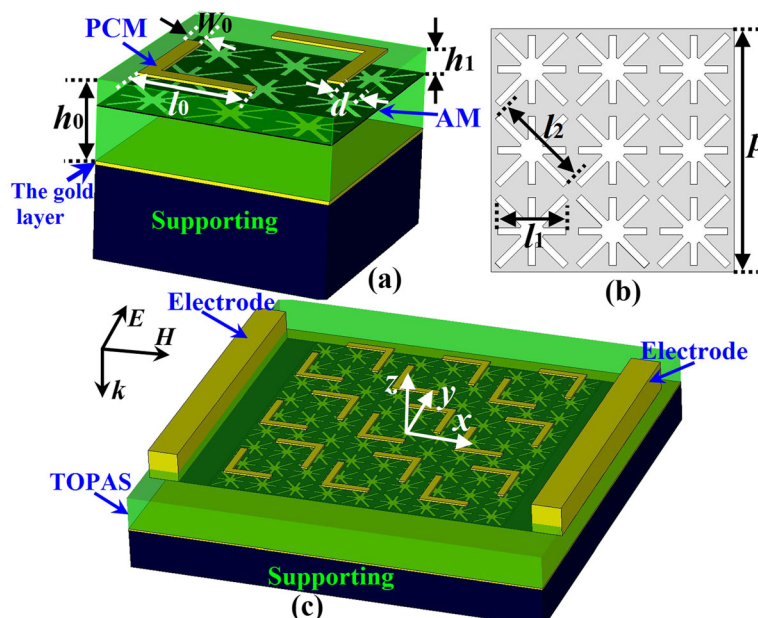


Fig. 2 Schematic view of the proposed MFD with absorbance and polarization conversion modes. **a** 3D view of a cell. **b** Top view of the graphene AM in one cell. **c** 3D view of the array

analyses are conducted in CST Studio Suite with frequency domain solver. Therefore, unit cell boundaries are set at the periphery sides, and a floquet port is set at the top of the calculation region. The PCR and absorptivity of the structure without AM are also plotted in the figure for comparison. Note that the PCR and absorptivity can be calculated through the reflection coefficients of the structure since there is no transmission owing to the gold layer [34]. Here, the terms are explicitly defined according to y -polarized illumination. The electric field of the y -polarized incidence wave is defined as E_{iy} , and the reflected wave includes a y -polarized electric field (E_{ry}) and x -polarized electric field (E_{rx}). Then, the reflection coefficients of co-polarization and cross-polarization are defined as $r_{yy} = E_{ry}/E_{iy}$ and $r_{xy} = E_{rx}/E_{iy}$, respectively. Therefore, the PCR and absorptivity can be calculated by Eqs. (2) and (3), respectively. Note that the PCR and absorptivity of x -polarized incidence can be analogously calculated according to Eqs. (2) and (3).

$$\text{PCR} = r_{xy}^2 / (r_{yy}^2 + r_{xy}^2) \quad (2)$$

$$\text{Abs.} = 1 - r_{yy}^2 - r_{xy}^2 \quad (3)$$

As shown in Fig. 3b, the MFD operates at PC mode with $\mu_c = 0$ eV, and it works at absorption mode with $\mu_c = 0.7$ eV. At the PC mode, the structure operates as a polarization converter, and it rotates a linear polarized incident wave to its orthogonal polarization wave. For the PC mode, the PCR is larger than 0.9 in the 2.11–3.63-THz band (53.0% at 2.87 THz), while the absorptivity is small and it ranges from 0.14 to 0.27 in the band. For the structure without AM, it has almost the same PCR band as the PC mode while its absorptivity ranges from 0.06 to 0.09. In the absorption mode, most of the incident wave is

absorbed in the band as demonstrated in the figure. Note that the PCR curve for absorption mode is not presented as it is meaningless. The absorptivity is larger than 80% in the 1.59–4.54-THz band (96.4% at 3.06 THz). Therefore, by adjusting the chemical potential, the proposed structure can switch between PC mode and absorption mode.

Physical Mechanisms

To further reveal the physical mechanisms of the switching characteristics of the two modes, the electric energy densities at the PC mode and the absorption mode of the structure are presented in Figs. 4 and 5, respectively. The current distributions of the PC mode are also plotted in Fig. 4 to state the polarization conversion characteristic. The current distributions of the absorption mode are not illustrated as the currents are attenuated and dissipated at this mode. Note that the field distributions are obtained under y -polarized illuminations.

For the PC mode ($\mu_c = 0$ eV), two frequencies of 2.56 THz and 3.22 THz are chosen to present their field distributions at Fig. 4a and b, respectively. The left parts of the figures are the electric energy densities, and the right parts are the currents. As shown in the figures, the field distributions of 2.56 THz and 3.22 THz are very similar to each other, which imply a wide operating band. From the electric energy densities at the left parts of Fig. 4a, b, the energies are mainly concentrated on the L-shaped structures (PCM). It is indicated that the PCM plays a leading role for $\mu_c = 0$ eV. From the currents at the right parts of Fig. 4a, b, the currents of both 2.56 THz and 3.22 THz are also concentrated on the PCM, and the currents on the AM are weak. The dotted line arrows indicate the vectors of the currents. The y -polarized illuminations generate x -vector currents on the L-shaped structures, which achieve polarization conversion.

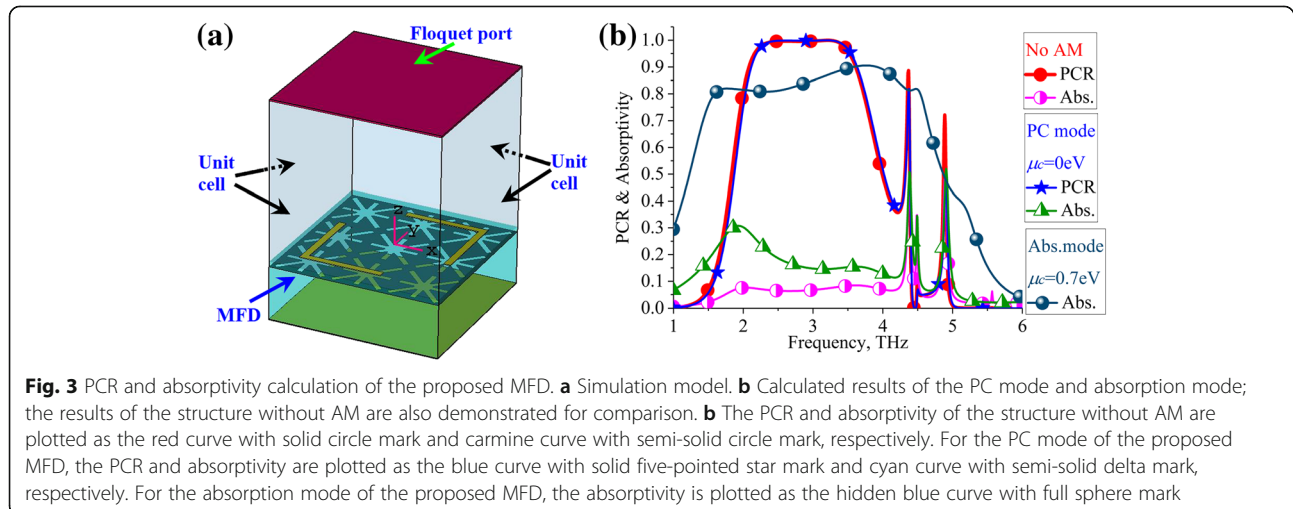


Fig. 3 PCR and absorptivity calculation of the proposed MFD. **a** Simulation model. **b** Calculated results of the PC mode and absorption mode; the results of the structure without AM are also demonstrated for comparison. **b** The PCR and absorptivity of the structure without AM are plotted as the red curve with solid circle mark and carmine curve with semi-solid circle mark, respectively. For the PC mode of the proposed MFD, the PCR and absorptivity are plotted as the blue curve with solid five-pointed star mark and cyan curve with semi-solid delta mark, respectively. For the absorption mode of the proposed MFD, the absorptivity is plotted as the hidden blue curve with full sphere mark

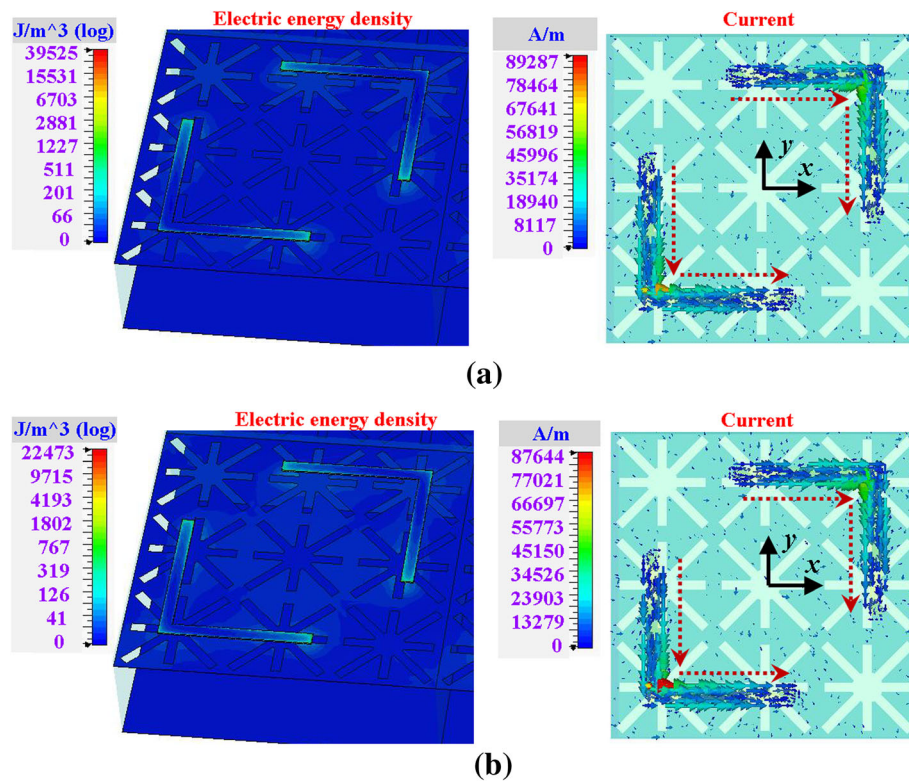


Fig. 4 Field distributions of the PC mode ($\mu_c = 0$ eV). **a** 2.56 THz. **b** 3.22 THz

For the absorption mode ($\mu_c = 0.7$ eV), the electric energy densities of 1.7 THz and 3.3 THz are painted in Fig. 5a and b, respectively. As shown in the figure, the electric energy densities of the two frequencies are mainly distributed on the AM. It is also found that the energies are focused in the cross-slot patterns; therefore, SPP effects are enhanced by the cross-slots on the AM. The strong SPP effects lead to field enhancement on the AM, which endow the AM a dominant role. Thereby, the incident waves are confined and dissipated in the AM. It is also

found that there are still some energies spread on the PCM, which make no perfect absorption, such as 80–90% absorptivity in the band.

Discussion

To further reveal the characteristics of the proposed MFD, parametric studies are discussed in this section. Figure 6a and b present the PCR and absorption characteristics, respectively, in terms of the chemical potential (μ_c). As shown in Fig. 6a, a smaller μ_c means smaller

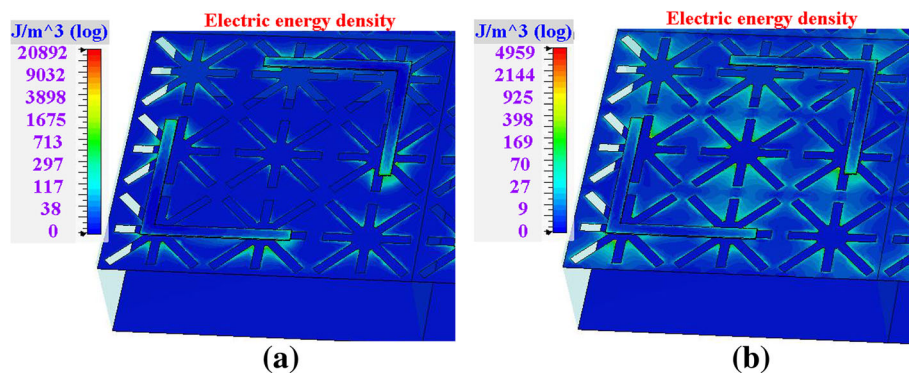


Fig. 5 Field distributions of the absorption mode ($\mu_c = 0.7$ eV). **a** 1.7 THz. **b** 3.3 THz

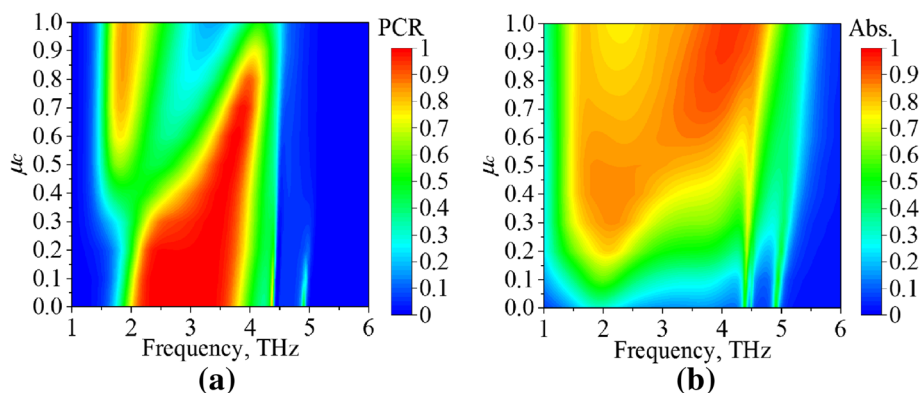


Fig. 6 Characteristics of the proposed MFD for different chemical potentials (μ_c). **a** PCR. **b** Absorption

conductivity of the AM, and the PCM has a stronger role. Therefore, good PCR is observed with $\mu_c = 0$ eV, and it is deteriorated with increasing μ_c . The absorption characteristic of the MFD presents almost contrary tendency as shown in Fig. 6b. With μ_c increased from 0 to 1 eV, the SPPs on the AM are inspired and enhanced. Thus, the incident EM waves are confined in the AM, and the power is absorbed. The $\mu_c = 0.7$ eV is chosen for the widest bandwidth. It is also noticed in Fig. 6a that the PCR values around 1.85 THz are larger than 80% for $0.7 \text{ eV} < \mu_c < 1 \text{ eV}$; however, most of the powers are dissipated for these μ_c s as indicated in Fig. 6b. Therefore, the chemical potential (μ_c) is a valuable parameter to adjust the PCR and absorption characteristics.

The absorptivity of the absorption mode for different polarization angles (ϕ_1 and ϕ_2) is depicted in Fig. 7. As

depicted in Fig. 7a, the ϕ_1 and ϕ_2 are the angles of the incident electric fields relative to x - and y -axes, respectively. According to the symmetric structure of the MFD, the ϕ_1 and ϕ_2 varied from 0 to 45° . In Fig. 7b, as the ϕ_1 increased from 0 to 45° , the absorptivity in the band increased from 0.8 to nearly 1, though the band is narrowed a bit with increasing ϕ_1 . As exhibited in Fig. 7c, the increasing of ϕ_2 debases the absorptivity around 2–3 THz, and two absorption bands are obtained around 1.7 THz and 4 THz.

The performances of PC mode and absorption mode in terms of incident angle (θ) are presented in Figs. 8 and 9, respectively. Figure 8a and b demonstrate the PCR plots of s - and p -polarized incident waves, respectively, with the incident angle ranged from 0 to 80° . As shown in the figures, the PCR deteriorated with increasing θ ; however, good PCR characteristic is also obtained for θ smaller than

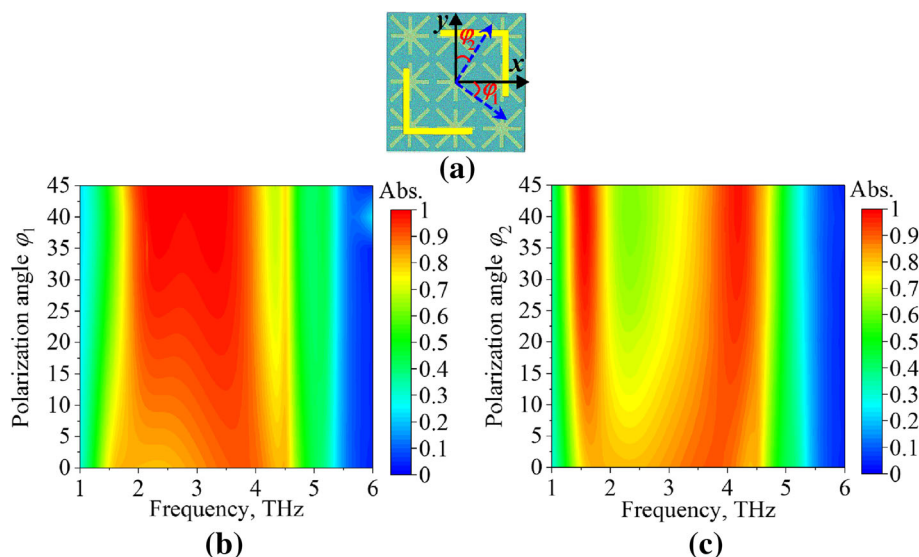


Fig. 7 The absorption characteristics of the absorption mode ($\mu_c = 0.7$ eV) under normal incidence for different polarization angles (ϕ). **a** The ϕ_1 and ϕ_2 are the angle of the incident electric field relative to x - and y -axes, respectively. **b** ϕ_1 . **c** ϕ_2

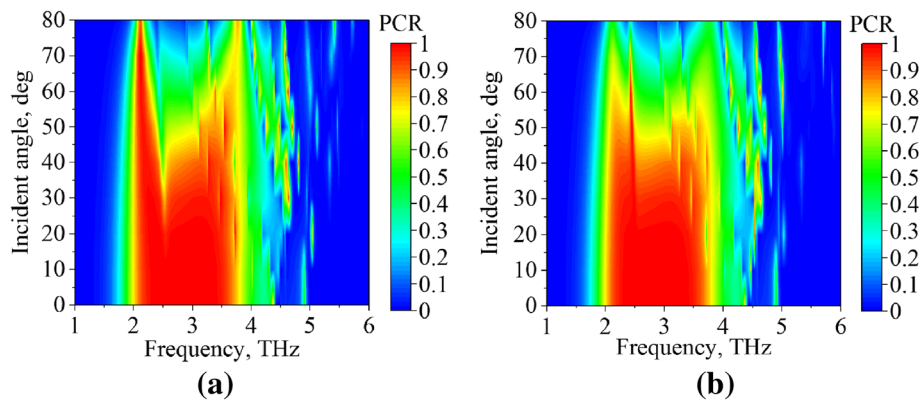


Fig. 8 The PCR characteristics of PC mode ($\mu_c = 0$ eV) for different incident angles, illuminated by **a** *s*-polarized and **b** *p*-polarized waves

40°. The PCR bandwidth is stable to the incident angle (θ). It is also found that the PCR performance of *s*-polarized incidence is insensitive to the incident angle (θ) for the frequencies around 2.1 THz.

For the absorption mode, the absorptivity plots of *s*- and *p*-polarized incident waves are plotted in Fig. 9a and b, respectively, with the incident angle (θ) ranged from 0 to 80°. Generally speaking, the absorptivity of the *s*-polarized incidence reduced with increasing θ , and the absorptivity is larger than 0.8 for θ smaller than 30°. It is interesting to find that the absorptivity of *p*-polarized incident EM wave increased with increasing θ .

The structure parameter h_1 is also studied to further reveal the multiple functions of the device. As the h_1 is adjusted, the position of the AM is changed. Note that other structure parameters are not discussed here for simplicity. Figure 10a and b demonstrate the results of the PC mode and absorption mode, respectively. As shown in the left part of Fig. 10a, at PC mode, the h_1 has little impact on the PCR. In the right part of Fig. 10b, the absorptions are also stable for h_1 ranging from 0.5 to 16.5 μm , though

smaller h_1 has larger absorption. The results in Fig. 10a verify the discussions in the “Methods” section, and the AM is operated as thin substrate at PC mode ($\mu_c = 0$ eV). For the absorption mode ($\mu_c = 0.7$ eV), the AM plays a leading role; therefore, the h_1 is important at this mode. As shown in the left part of Fig. 10a, the increasing of h_1 decrease the absorptivity. It is because the multiple reflections and superpositions between the AM and the gold layer are important to inspire the SPPs and enhance the fields on the AM [35]. In the right part of Fig. 10b, good PCR is observed for larger h_1 . Therefore, in the designing of the MFD, the parameter h_1 can be only considered in the absorption mode as it has little impact on the PC mode.

Conclusions

In summary, a low-profile and simple structure MFD is proposed by combining gold-based PCM and graphene-based AM. The chemical potential (μ_c) can be utilized to activate or neutralize the graphene-based AM, and then, the structure can be transformed from absorber

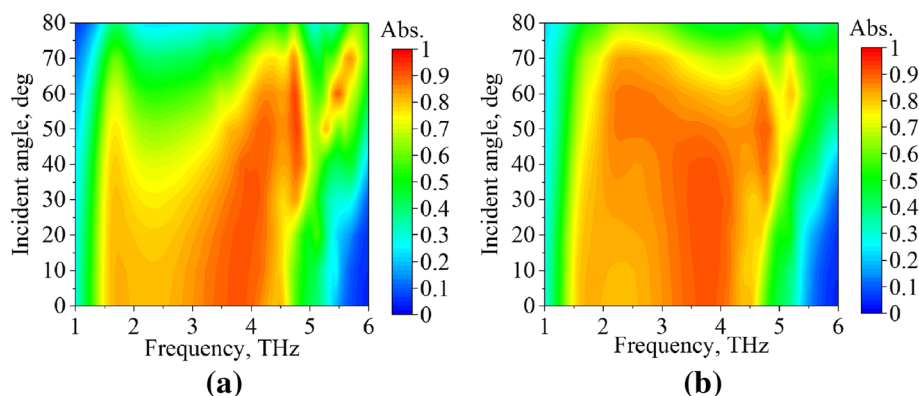


Fig. 9 The absorption characteristics of absorption mode ($\mu_c = 0.7$ eV) for different incident angles, illuminated by **a** *s*-polarized and **b** *p*-polarized waves

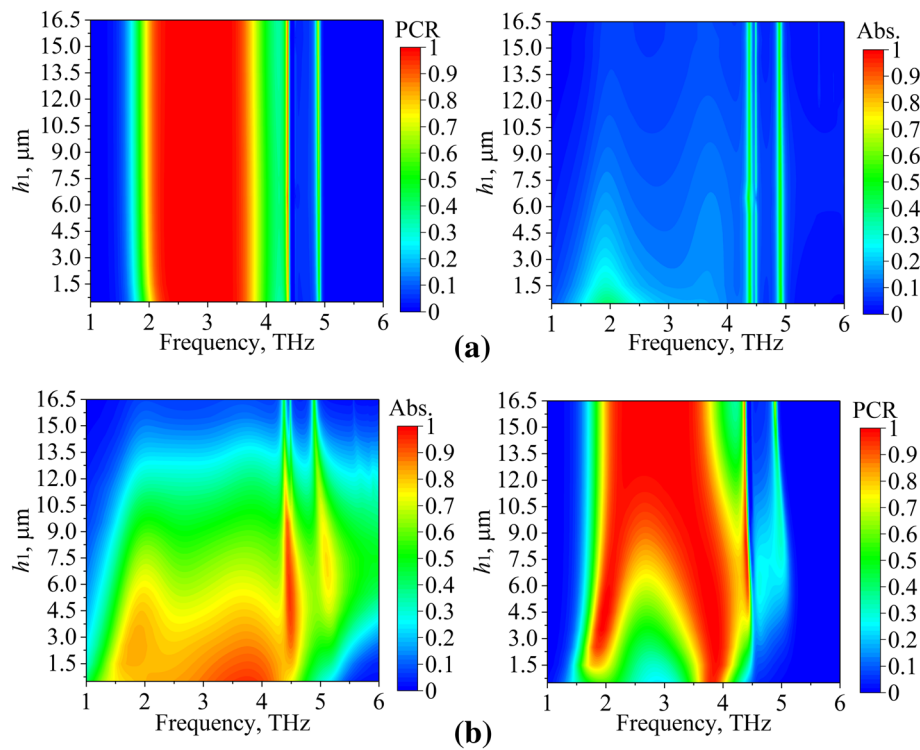


Fig. 10 The PCR and absorption in terms of h_1 . **a** PC mode ($\mu_c = 0$ eV). **b** Absorption mode ($\mu_c = 0.7$ eV)

to polarization converter. For the PC mode, the PCR is larger than 0.9 in the 2.11–3.63-THz band (53.0% at 2.87 THz). For the absorption mode, the absorptivity is larger than 80% in the 1.59–4.54-THz band (96.4% at 3.06 THz). The design may be applied to terahertz imaging, sensing, photodetection, and modulation systems.

Abbreviations

AM: Absorbing metasurface; CP: Circular polarization; EM: Electromagnetic; LP: Linear polarization; MFD: Multi-functional device; PC: Polarization conversion; PCM: Polarization conversion metasurface; PCR: Polarization conversion ratio; SPPs: Surface plasmon polaritons

Acknowledgements

Not applicable.

Funding

National Natural Science Foundation of China under Grant Nos. 61661011 and 61761012.

Availability of Data and Materials

The datasets used and/or analyzed during the current study are available from the corresponding author on reasonable request.

Authors' Contributions

LP developed the concept. LP conducted the simulations. LP, JX, and SML analyzed the results and physical mechanisms. All authors reviewed the manuscript. All authors read and approved the final manuscript.

Competing Interests

The authors declare that they have no competing interests.

Publisher's Note

Springer Nature remains neutral with regard to jurisdictional claims in published maps and institutional affiliations.

Author details

¹Guangxi Key Laboratory of Wireless Wideband Communication and Signal Processing, Guilin University of Electronic Technology, Guilin 541004, Guangxi, China. ²School of Physics, University of Electronic Science and Technology of China, Chengdu 541004, China. ³Guangxi University of Science and Technology, Liuzhou 545006, Guangxi, China.

Received: 19 September 2018 Accepted: 19 November 2018

Published online: 29 November 2018

References

1. Tonouchi M (2007) Cutting-edge terahertz technology. *Nat Photonics* 1(2): 97–105
2. Jepsen PU, Cooke DG, Koch M (2011) Terahertz spectroscopy and imaging—modern techniques and applications. *Laser Photonics Rev* 5(1):124–166
3. Song ZY, Gao Z, Zhang YM, Zhang BL (2014) Terahertz transparency of optically opaque metallic films. *Europhys Lett* 106(2):27005
4. Yu P, Besteiro LV, Huang Y, Wu J, Fu L, Tan HH, et al (2018) Broadband metamaterial absorbers. *Adv Opt Mater* 0(0):1800995. <https://doi.org/10.1002/adom.201800995>
5. Landy NI, Bingham CM, Tyler T, Jokerst N, Smith DR, Padilla WJ (2009) Design, theory, and measurement of a polarization-insensitive absorber for terahertz imaging. *Phys Rev B* 79(12):125104
6. Liu X, Starr T, Starr AF, Padilla WJ (2010) Infrared spatial and frequency selective metamaterial with near-unity absorbance. *Phys Rev Lett* 104(20):207403
7. Cui YX, He YR, Jin Y, Ding F, Yang L, Ye YQ, Zhong SM, Lin YY, He SL (2014) Plasmonic and metamaterial structures as electromagnetic absorbers. *Laser Photonics Rev* 8(4):495–520
8. Alaei R, Albooyeh M, Rockstuhl C (2017) Theory of metasurface based perfect absorbers. *J Phys D Appl Phys* 50(50):503002

9. Grant J, Ma Y, Saha S, Khalid A, Cumming DR (2011) Polarization insensitive, broadband terahertz metamaterial absorber. *Opt Lett* 36:3476–3478
10. Pham PH, Zhang W, Quach NV, Li J, Zhou W, Scarmardo D, Brown ER, Burke PJ (2017) Broadband impedance match to two-dimensional materials in the terahertz domain. *Nat Commun* 8(1):2233
11. Lv H, Guo Y, Zhao Y, Zhang H, Zhang B, Ji G, Xu ZJ (2016) Achieving tunable electromagnetic absorber via graphene/carbon sphere composites. *Carbon* 110:130–137
12. Andryieuski A, Lavrinenko AV (2013) Graphene metamaterials based tunable terahertz absorber: effective surface conductivity approach. *Opt Express* 21: 9144–9155
13. Mou N, Sun S, Dong H, Dong S, He Q, Zhou L, Zhang L (2018) Hybridization-induced broadband terahertz wave absorption with graphene metasurfaces. *Opt Express* 26(9):11728–11736
14. Xu Z, Wu D, Liu Y, Liu C, Yu Z, Yu L, Ye H (2018) Design of a tunable ultra-broadband terahertz absorber based on multiple layers of graphene ribbons. *Nanoscale Res Lett* 13(1):143
15. Amin M, Farhat M, Bağcı H (2013) An ultra-broadband multilayered graphene absorber. *Opt Express* 21(24):29938–29948
16. Li HJ, Ren YZ, Hu JG, Qin M, Wang LL (2018) Wavelength-selective wide-angle light absorption enhancement in monolayers of transition-metal dichalcogenides. *J Lightwave Technol* 36(16):3236–3241
17. Huo DW, Zhang JW, Wang H, Ren XX, Wang C, Su H, Zhao H (2017) Broadband perfect absorber with monolayer MoS₂ and hexagonal titanium nitride nano-disk array. *Nanoscale Res Lett* 12(1):465
18. Gao X, Singh L, Yang WL, Zheng J, Li H, Zhang W (2017) Bandwidth broadening of a linear polarization converter by near-field metasurface coupling. *Sci Rep* 7:6817
19. Jing X, Gui X, Zhou P, Hong Z (2018) Physical explanation of Fabry–Pérot cavity for broadband bilayer metamaterials polarization converter. *J Lightwave Technol* 36(12):2322–2327
20. Fartookzadeh M (2017) Design of metamirrors for linear to circular polarization conversion with super-octave bandwidth. *J Mod Opt* 64(18):1854–1861
21. Peng L, Li XF, Jiang X, Li SM (2018) A novel THz half-wave polarization converter for cross-polarization conversions of both linear and circular polarizations and polarization conversion ratio regulating by graphene. *J Lightwave Technol* 36(19):4250–4258
22. Ding J, Arigong B, Ren H, Shao J, Zhou M, Lin Y, Zhang H (2015) Mid-infrared tunable dual-frequency cross polarization converters using graphene-based L-shaped nanoslot array. *Plasmonics* 10(2):351–356
23. Yang C, Luo Y, Guo J, Pu Y, He D, Jiang Y, Liu Z (2016) Wideband tunable mid-infrared cross polarization converter using rectangle-shape perforated graphene. *Opt Express* 24(15):16913–16922
24. Cheng H, Chen S, Yu P, Li J, Deng L, Tian J (2013) Mid-infrared tunable optical polarization converter composed of asymmetric graphene nanocrosses. *Opt Lett* 38(9):1567–1569
25. You JW, Panoiu NC (2018) Polarization control using passive and active crossed graphene gratings. *Opt Express* 26(2):1882–1894
26. Hanson GW (2008) Dyadic Green's functions and guided surface waves for a surface conductivity model of graphene. *J Appl Phys* 103(6):064302
27. Falkovsky LA (2008) Optical properties of graphene. *J Phys Conf Ser* 129(1):012004
28. Lim GK, Chen ZL, Clark J, Goh RG, Ng WH, Tan HW, Friend RH, Ho PK, Chua LL (2011) Giant broadband nonlinear optical absorption response in dispersed graphene single sheets. *Nat Photonics* 5:554–560
29. Bonaccorso F, Sun Z, Hasan T, Ferrari AC (2010) Graphene photonics and optoelectronics. *Nat Photonics* 4:611–622
30. Tang HH, Huang TJ, Liu JY, Tan Y, Liu PK (2017) Tunable terahertz deep subwavelength imaging based on a graphene monolayer. *Sci Rep* 7:46283
31. Cunningham PD, Valdes NN, Vallejo FA, Hayden LM, Polishak B, Zhou XH, Luo JD, Jen AKY, Williams JC, Twieg RJ (2011) Broadband terahertz characterization of the refractive index and absorption of some important polymeric and organic electro-optic materials. *J Appl Phys* 109(4):043505
32. Yan HG, Li XS, Chandra B, Tulevski G, Wu YQ, Freitag M, Zhu WJ, Avouris P, Xia FN (2012) Tunable infrared plasmonic devices using graphene/insulator stacks. *Nat Nanotechnol* 7(5):330
33. Zhang Y, Feng Y, Jiang T, Cao J, Zhao J, Zhu B (2018) Tunable broadband polarization rotator in terahertz frequency based on graphene metamaterial. *Carbon* 133:170–175
34. Menzel C, Rockstuhl C, Lederer F (2010) Advanced Jones calculus for the classification of periodic metamaterials. *Phys Rev A* 82(5):053811
35. Chen HT (2012) Interference theory of metamaterial perfect absorbers. *Opt Express* 20(7):7165–7172

Submit your manuscript to a SpringerOpen[®] journal and benefit from:

- Convenient online submission
- Rigorous peer review
- Open access: articles freely available online
- High visibility within the field
- Retaining the copyright to your article

Submit your next manuscript at ► [springeropen.com](https://www.springeropen.com)